Glacial and hydrothermal sources of dissolved iron(II) in Southern Ocean waters surrounding Heard and McDonald Islands

Thomas M. Holmes[1,2,†], Kathrin Wuttig[1], Zanna Chase[2], Christina Schallenberg[1], Pier van der Merwe[1], Ashley T. Townsend[3], and Andrew R. Bowie[1,2]

[1]Antarctic Climate and Ecosystems Cooperative Research Centre (ACE CRC), University of Tasmania, Private Bag 80, Hobart, Tasmania 7001, Australia.

[2]Institute for Marine and Antarctic Studies (IMAS), University of Tasmania, Private Bag 129, Hobart, Tasmania, Australia.

[3]Central Science Laboratory (CSL), University of Tasmania, Private Bag 74, Hobart, TAS 7001, Australia.

Corresponding author: Thomas M. Holmes (Thomas.holmes@utas.edu.au)

†Current address: School of Oceanography, University of Washington, Box 357940, Seattle, WA 98105, USA.

Key Points:

- Remote Heard and McDonald Islands are distinct iron(II) sources in the Southern Ocean
- The main iron(II) source at Heard Island is glacial, while hydrothermal vents are the main source of iron(II) near McDonald Islands
- Dissolved iron(II) and peroxide data are successfully utilised to resolve iron sources in a well-mixed and oceanographically complex system

Deleted: Results

Deleted: highlight complex iron cycling at a Southern Ocean biological hotspot, with implications for regional bioavailability of iron

Abstract

The Southern Ocean is the largest region in which iron limits the growth of phytoplankton. However, a phytoplankton bloom thousands of square kilometres in area forms each spring-summer in the Indian sector of the Southern Ocean, both above and to the east of the Kerguelen Plateau. The central region of the Kerguelen Plateau hosts the volcanically active islands, Heard and McDonald (HIMI), the former of which is largely covered by glaciers. The sources and processes governing supply of iron from HIMI to the region are relatively unknown. In the austral summer of 2016, the first voyage to focus on biogeochemical cycling in the HIMI region was undertaken (GEOTRACES process study GIpr05). Using dissolved iron(II) (DFe(II)) and peroxide measurements, we are able to resolve iron sources and show that each of the adjacent islands are strong sources of reduced iron, though controlled by different supply mechanisms.

At Heard Island, the greatest DFe(II) concentrations (max 0.57 nmol L^{-1}) were detected north of the island. An inverse correlation of DFe(II) concentrations with salinity suggests the origin is from a sea-terminating glacier on the island. At McDonald Islands, the greatest DFe(II) concentrations (max 1.01 nmol L^{-1}) were detected east of the islands which, based on DFe(II) profiles from five targeted stations, appears likely to originate from shallow diffuse hydrothermalism. Elevated DFe(II) around HIMI may increase Fe availability for biota and have implications for transport of Fe away from the islands to the broader northern Kerguelen Plateau where the annual plankton bloom is strongest.

Plain language summary

Phytoplankton form the base of the aquatic food web, produce comparable atmospheric oxygen to terrestrial plants and help moderate global heating through uptake of CO_2. Thus, it is vital to know what influences phytoplankton growth in the ocean. Along with nutrients such as nitrate and phosphate, phytoplankton require iron for growth. Iron concentrations are

very low in the Southern Ocean, limiting the growth of phytoplankton. However, near the Kerguelen Plateau in the Indian sector of the Southern Ocean, a phytoplankton bloom thousands of square kilometres in area forms each spring-summer. There are two volcanically active islands in the central region of the Kerguelen Plateau – Heard and McDonald. Volcanic activity supplies iron in various forms to the ocean, yet these islands have not been studied in detail. Iron(II) is a short-lived yet preferred form of iron for phytoplankton in the ocean. Using iron(II), we show that these closely spaced islands supply iron in different ways. Underwater volcanic vents supply iron near McDonald Island, while glacial runoff supplies iron near Heard Island. Knowing these iron sources is essential for understanding what causes this large phytoplankton bloom at the Kerguelen Plateau, an important ecological hotspot and contributor for regulation of atmospheric CO_2.

1. Introduction

Iron (Fe) is a key limiting, or co-limiting, micronutrient for biological primary production (Martin et al., 1990) in as much as half of the world's oceans (Moore et al., 2009), with important implications for biogeochemical cycling and the drawdown of carbon from the atmosphere (Boyd and Ellwood, 2010). The most energetically stable form of Fe in the oxygenated ocean, Fe(III), has low solubility. The reduced form of Fe, Fe(II), is more soluble in seawater and should be kinetically more bioavailable to phytoplankton (Shaked et al., 2005). However, Fe(II) is only present as a transient species in the oxygenated ocean, generally existing in vanishingly low concentrations (picomolar or less) due to rapid (minutes to days) oxidation by oxygen (O_2) and hydrogen peroxide (H_2O_2) in surface waters (Millero et al., 1987).

Nevertheless, continuous production of Fe(II) by several processes in the ocean can lead to measurable quantities in both surface and deeper waters. In the surface ocean, concentrations of Fe(II) are increased by photochemical reduction of organic-Fe(III) complexes (Rijkenberg

et al., 2005), wet and dry atmospheric deposition (Croot and Heller, 2012), glacial melt in higher latitudes (Raiswell et al., 2018 and references therein) and biological production by processes such as viral lysis of cells (Gobler et al., 1997) and grazing (Hutchins and Bruland, 1994). In the deeper ocean and on continental shelves, sources include benthic fluxes from anoxic and sub-oxic sediments (Lohan and Bruland, 2008), hydrothermal fluids (Holmes et al., 2017; Sedwick et al., 2015) and redox cycling induced by oxygen minimum zones (Lohan and Bruland, 2008). Thus, given the rapid loss of Fe(II) in oxygenated seawater, measurements of Fe speciation can be used as a near-field tracer of processes and sources of Fe biogeochemistry in the ocean (Holmes et al., 2017).

The oxidation kinetics of Fe(II) in seawater are complex, depending on many factors including pressure, temperature, salinity, O_2 concentration, H_2O_2 concentration and pH (Millero et al., 1987; Millero and Sotolongo, 1989; Santana-Casiano et al., 2006). At the pH of seawater, the oxidation rate of Fe(II) is heavily dependent on O_2 and H_2O_2 concentrations, with the relative influence of each species dependent on its concentration (Santana-Casiano et al., 2006). Rainwater and biological production can contribute to the H_2O_2 inventory (Croot et al., 2004). Rainwater scavenges H_2O_2 from the atmosphere (Cohan et al., 1999), increasing surface ocean concentrations through direct deposition; however, this process is more prevalent in lower latitudes (Weller and Schrems, 1993). Studies have also demonstrated biological production of H_2O_2 in the water column (Palenik and Morel, 1988) but the major source of H_2O_2 in the ocean is through photochemical reactions involving dissolved organic matter and O_2 (Croot et al., 2004). When concentrations of H_2O_2 are less than 200 nmol L^{-1}, Fe(II) is at nanomolar levels and pH is 8, O_2 becomes the most important oxidant (Santana-Casiano et al., 2006). Therefore, it is important to consider both of these oxidants when analysing Fe(II) cycling.

99 The Southern Ocean (SO) is the largest region of Fe deficiency in the World's oceans (Boyd
100 et al., 2007). However, within the Indian sector of the SO, there is an oasis of relatively Fe
101 rich waters overlaying the Kerguelen Plateau. At the southern part of the central Kerguelen
102 plateau is an active volcanic hotspot, hosting two active subaerial volcanic islands, Heard and
103 McDonald (HIMI), the former of which is largely covered by glaciers. Waters in the region
104 are subject to an intense mixing regime, caused by strong winds, shallow bathymetry
105 characterised by many seamounts and ridges, and the location of the plateau in the path of
106 strong currents associated with the polar front to the north and Fawn Trough Current to the
107 south of HIMI (Figure 1; Park et al., 2014). Fed by the Fe-rich waters formed on the plateau,
108 a plankton bloom on the order of thousands of square kilometres forms over and downstream
109 of the plateau each spring and summer (Blain et al., 2008). In the austral summer of 2016, the
110 first voyage to focus on biogeochemical cycling in the HIMI region was undertaken: Heard
111 Earth-Ocean-Biosphere Interactions (HEOBI). In the context of an interdisciplinary study
112 centred around hydrothermalism, we measured dissolved Fe(II) (DFe(II)) and hydrogen
113 peroxide (H_2O_2) to uncover which sources and processes were important for the distribution
114 and oxidation kinetics of DFe(II) around HIMI, with implications for Fe bioavailability and
115 transport of Fe to the northern plateau.

116 **2. Methods**

117 2.1. Study area

118 Sampling and shipboard analyses were carried out aboard R/V *Investigator* during the
119 HEOBI voyage (GEOTRACES process study GIpr05) from January 8th to February 27th 2016
120 around Heard and McDonald Islands (HIMI) on the Kerguelen Plateau in the Indian sector of
121 the SO. Twenty-seven stations were successfully sampled for both DFe(II) and H_2O_2 (Figure
122 1), with an extra four stations sampled for H_2O_2 only (not shown). The same locations were

123 also occupied by Conductivity-Temperature-Depth rosette (CTD) casts, along with an

124 additional 22 CTD only stations (not shown).

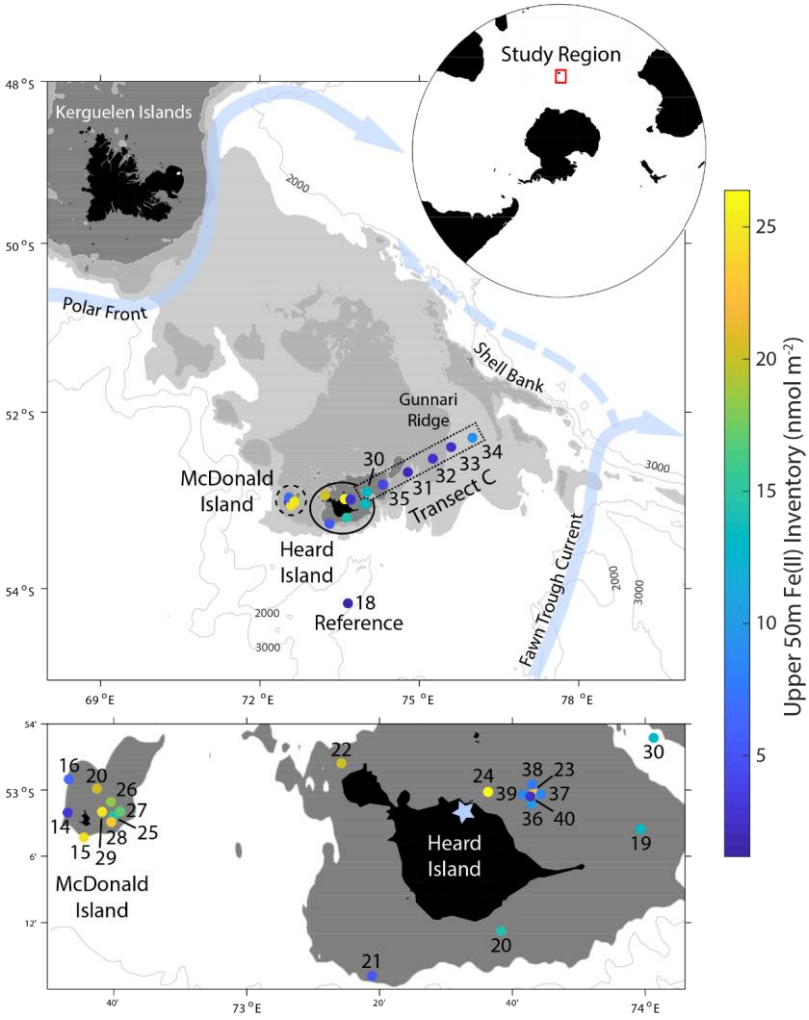

125

126 Figure 1. DFe(II) integrated inventory in the upper 50 m at each station sampled for DFe(II) during HEOBI. Concentrations
127 indicated by colour bar. TMR station numbers and regions are annotated. Location of study region is shown in top inset.
128 Heard and McDonald Islands are shown zoomed in bottom inset. Transect C (dotted square) follows the first 150 km of
129 'Transect C' from a previous voyage (Kerguelen Ocean and Plateau Compared Study: KEOPS-1; Blain et al., 2008). The
130 reference station was located to the south of HIMI in high-nutrient, low chlorophyll (HNLC) waters. Bathymetric isobaths
131 are shown, with seabed <200 m depth shaded dark grey, <500 m shaded lighter grey and <1000 m shaded lightest grey.
132 Major currents are shown in light blue arrows, adapted from Park et al., (2014). Downes and Ealey marine terminating
133 glaciers are marked by a blue star on Heard Island.

Sample stations were divided into 4 regions: Transect C, Heard Island, McDonald Islands and reference stations. Transect C was oriented in a northeast-southwest direction, with the aim of highlighting the near shore to deep water gradient in biogeochemical tracers. Transect C extends from Heard Island across Gunnari Ridge towards Shell Bank, crossing almost perpendicular to the prevailing current, which flows northward along the plateau. This transect followed the same trajectory as the previous KEOPS-1 'C' transect in 2005 (Blain et al., 2008), though not reaching as far to the northeast as the previous transect, which extended off the plateau into waters >3500 m deep.

Sampling station locations in the HIMI region were selected based on bathymetric features (Watson et al., 2016) and acoustic flare signals detected with shipboard echosounders (Spain et al., 2019) suggesting potential hydrothermal activity (see section 3.1). Acoustic flare signals had distinct characteristics when caused by seafloor gas seepage (Spain et al., 2019). Based on these criteria, two sites were chosen for an additional five stations located in a crosshair pattern – one at McDonald Islands (stations 25 – 29) and one at Heard Island (stations 36 – 40) – in an attempt to further delineate possible hydrothermal inputs.

A reference site, (station 18) was sampled ~100 km to the south of Heard Island, located in waters more representative of HNLC conditions (max 0.81 mg m^{-3} Chl*a* in upper 200 m; Wojtasiewicz et al., 2019). Mean currents at this station were associated with the Fawn Trough Current, moving from west (open ocean) to east (plateau; Figure 1; Park et al., 2014).

2.2. Sample collection

Briefly, all water column samples were collected in 12 L Niskin bottles modified for trace metal sampling, deployed using the Australian Marine National Facility trace-metal-clean rosette (TMR) equipped with a Seabird CTD unit and attached to a Dyneema rope. Once recovered, the Niskin bottles were rapidly transferred into a trace-metal-clean containerised

laboratory for sub-sampling and sample processing. All sample manipulation and analyses were conducted following GEOTRACES guidelines (Cutter et al., 2014) under ISO 5 HEPA filtered air within the containerised clean room. Both DFe(II) and H_2O_2 samples were collected in acid-cleaned, dark brown (low-light transmittance), high-density polyethylene (Nalgene) sample bottles. Dissolved Fe(II) samples were filtered through acid-washed Pall Acropak Supor capsule filters (0.2 µm) while samples for H_2O_2 were not filtered. Samples were immediately double bagged and put directly on ice. Samples were then transported into a separate trace metal clean analytical container for immediate analysis (DFe(II) within 1 hour, H_2O_2 within 2 hours). To ensure that any oxidation of DFe(II) which occurred between subsampling and analysis was consistent, every effort was made to keep the time between subsampling and analysis as consistent as possible at each station.

2.3. Dissolved iron(II) analysis

Dissolved Fe(II) samples were analysed using flow injection - chemiluminescence analysis (FIA-CL) with in-line preconcentration onto an 8-HQ resin adapted from the method of Bowie et al., (2005, 2002) and recently described by Sedwick et al., (2015). Briefly, a 0.02 mol L^{-1} DFe(II) stock solution was prepared before the voyage by dissolving trace metal grade ammonium iron(II) sulfate hexahydrate (Aldrich) in 0.1 µmol L^{-1} ultrapure hydrochloric acid (Seastar Baseline) solution. The stock solution was kept in darkness for the duration of the voyage. Working solutions of 200 µmol L^{-1} and 200 nmol L^{-1} concentrations were prepared daily via serial dilution with 0.1 mol L^{-1} HCl. All DFe(II) stock solutions contained sodium sulphite as a stabilising agent. Calibration standards were also prepared daily from the stock solution, in aged low-Fe seawater, buffered with 0.4 µmol L^{-1} ammonium acetate to a pH of ~6. Calibration standards covered a concentration range of 0 – 1.2 nmol L^{-1} (which was adequate for the majority of samples collected) and were analysed before each block of samples from individual stations.

The blank solution used for the DFe(II) FIA analysis consisted of low Fe seawater collected during the cruise. Triplicate blank measurements were taken both before and after each analysis sequence. Analysis times were recorded for each sample. For instances where instrument signal drift was noted between the initial and final blank measurements, a blank value was calculated for each sample via linear interpolation.

The detection limit of the DFe(II) FIA-CL instrument was defined as the analyte concentration equivalent to three times the standard deviation of the blank peak (n=3) (Bowie et al., 2005). During the HEOBI voyage the detection limit was calculated each day and ranged from 0.02 to 0.16 nmol L^{-1} with a mean of 0.06 nmol L^{-1} (n = 17).

2.4. Dissolved hydrogen peroxide analysis

Dissolved H_2O_2 samples were analysed using a FIA-CL reagent injection method (Yuan and Shiller, 1999). Briefly, H_2O_2 catalyses the chemiluminescence of luminol in the presence of Co^{2+} at alkaline pH. H_2O_2 standards were prepared by serial dilution from a 30% stock solution (Seastar Baseline) and were determined by spectrophotometric measurements with a 10 cm Liquid Waveguide Capillary Flow Cell (LWCC, World Precision Instruments, ε = 40.9 mol L^{-1} cm^{-1}; Hwang and Dasgupta, 1985). Each seawater sample was analysed at least four times with a typical precision of 3 – 5% through the concentration range 0.5 – 75 nmol L^{-1} and a typical detection limit (3σ) of 0.6 nmol L^{-1}.

2.5. Calculating dissolved iron(II) half-lives

Shipboard pH data was unavailable during HEOBI. Therefore, using in-situ O_2, H_2O_2, salinity, temperature and depth data, expected Fe(II) half-lives over the pH range 7.1 – 8.2 (the pH range of historical observations in the region, taken from the World Ocean Database; Tanhua et al., 2013) were calculated using a method modified from González-Dávila et al., (2006; and references therein). The overall rate of oxidation of Fe(II) is given by:

$$\frac{-dFe(II)}{dt} = k_{app,O_2}[Fe(II)][O_2] + k_{app,H_2O_2}[Fe(II)][H_2O_2] \quad (1)$$

where $k_{app,O2}$ and $k_{app,H2O2}$ are the apparent rate constants (M^{-1} min^{-1}) for oxidation by O_2 and H_2O_2, respectively. When oxidants are in excess, the reaction is pseudo first-order, and is given by:

$$\frac{-dFe(II)}{dt} = (k'_{O_2} + k'_{H_2O_2})[Fe(II)] \quad (2)$$

where k'_{O2} (min^{-1}) = $k_{app,O2}[O_2]$ and $k'_{[H2O2]}$ (min^{-1}) = $k_{app,h2O2}[H_2O_2]$. The overall half-life with respect to oxidation is:

$$T_{half} = 0.693(k'_{O_2} + k'_{H_2O_2})^{-1} \quad (3)$$

The k'_{O2} value was calculated following Millero et al. (1987) as follows:

$$\frac{-dFe(II)}{dt} = k'_{O_2}[Fe(II)] \quad (4)$$

where

$$k'_{O_2} = k[OH]^2[O_2] \quad (5)$$

The rate constant k can be calculated for a given temperature and ionic strength (see equations in Millero et al., 1987). Similarly, k'_{H2O2} was calculated according to Millero and Sotolongo (1989), with some assumptions:

$$\frac{-dFe(II)}{dt} = k'_{H_2O_2}[Fe(II)] \quad (6)$$

where

$$k'_{H_2O_2} = k[H_2O_2][OH^-] \quad (7)$$

These calculations assume that $[H_2O_2]>>[Fe(II)]$, which makes the oxidation of Fe(II) by H_2O_2 pseudo-first order. Calculated DFe(II) half-lives ranged between 30 minutes – 172 hours, decreasing with increasing pH (Figure S3)

2.6. Hydrographic data and dissolved iron data

Temperature, salinity, pressure and oxygen data were taken from Sea-Bird Electronics SBE3T, SBE4C, SBE9plus and SBE43 sensors respectively, which were mounted on the primary CTD rosette. Total dissolved iron (DFe) data, including collection and analysis methods are reported in Holmes et al., (2019).

3. Results

3.1. Dissolved Fe(II) distribution

3.1.1. Transect C

All Transect C stations were located above the plateau. The three most easterly stations (32, 33 and 34) had deep mixed layers, shoaling slightly towards the east (285, 254 and 245 m, respectively). Surface DFe(II) concentrations were low (mean upper 50 m concentrations, ≤ 0.15 nmol L^{-1}) compared to stations 30 and 23 at the western end of the transect (closer to HIMI), increasing to 0.29 and 0.44 nmol L^{-1} mean in the upper 50 m, respectively (Figure 2). A subsurface DFe(II) maximum was observed at Stations 31 – 34. Concentrations in this maximum layer decreased from 0.21 to 0.15 nmol L^{-1} between stations 31 to 34, while the depth of the layer increased from 97 to 297 m (Figure 2).

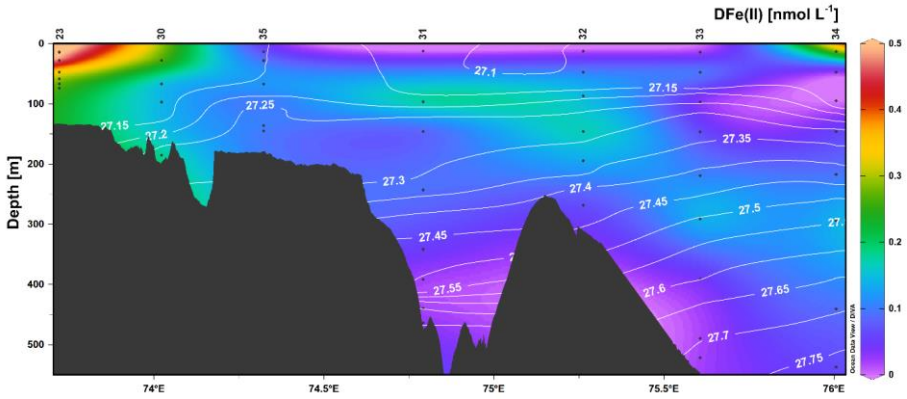

Figure 2. Transect C DFe(II) concentrations, with neutral density (γ^n; kg m^{-2}) surfaces overlaid (white lines, calculated from continuous CTD data). Black dots represent sample locations. Station numbers for TMR deployments are shown above the top axis.

3.1.2. Heard and McDonald Islands

Concentrations of DFe(II) were elevated around HIMI relative to transect and reference stations, with relatively homogeneous profiles throughout the water column (Figure 3). McDonald Islands had a significantly higher mean DFe(II) concentration (0.36 ± 0.16 nmol L^{-1}, n = 56) compared to Heard Island (0.24 ± 0.14 nmol L^{-1}, n = 57; *t*-test, $p<0.01$). At Heard Island, the maximum DFe(II) concentration (0.57 nmol L^{-1}) was located at station 24, north of the island and near Downes and Ealey marine-terminating glaciers. At McDonald Islands, the maximum DFe(II) concentration (1.01 nmol L^{-1}) was located to the east of the island. DFe(II) inventories calculated in the upper 50 m (minimum station depth at HIMI was ~48 m, measured at station 24) are shown in Figure 1, along with arrows showing general circulation features, adapted from Park et al., (2014). Stations to the south and east of Heard Island had lower DFe(II) inventories than stations to the north of Heard Island. Stations to the west of McDonald Islands had lower DFe(II) inventories than stations to the east of McDonald Islands. This distribution corresponds to higher concentrations on the shallower, plateau side of the islands.

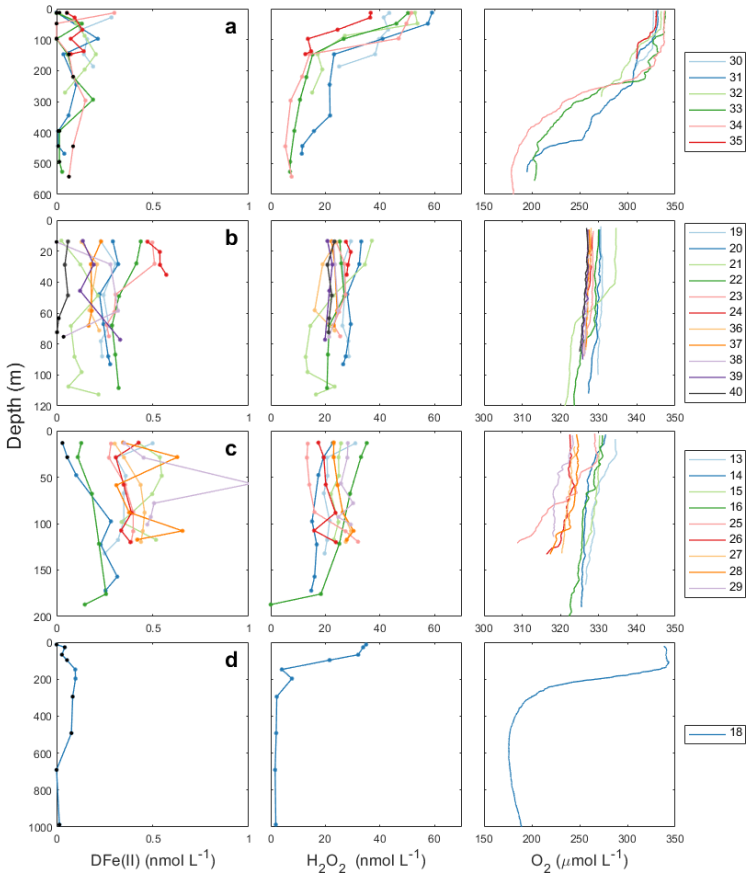

Figure 3. Profiles of DFe(II), H_2O_2 and O_2 for **a.** Transect C, **b.** Heard Island, **c.** McDonald Islands, and **d.** Reference station. Stations are colour coded and shown in legends on the right hand side of each region. Samples that were below the calculated detection limit for each station are shown in black. Note that O_2 x-axis scales vary.

3.1.3. Reference station

3.2. Surface DFe(II) concentrations were very low at reference station 18 (measured 0.03 ± 0.02 nmol L^{-1} mean in the upper 100m, n = 4, though two samples were below detection limit), increasing to a maximum (0.10 nmol L^{-1}) at 197 m before decreasing with depth (Figure 3). Dissolved H_2O_2 distribution

3.2.1. Transect C

Greater surface concentrations of H_2O_2 were observed at stations 31 – 34 (>48 nmol L^{-1}) towards the east of transect C compared to stations 35, 30 and 23 (41.9 – 25.3 nmol L^{-1}) towards the west of the transect, with the lowest surface concentration observed closest to HIMI at station 23 (Figure 4). The distribution of H_2O_2 closely followed density layers, with concentrations at stations 31 – 34 decreasing slightly with depth, while stations 35, 30 and 23 became increasingly homogenised over the water column towards HIMI.

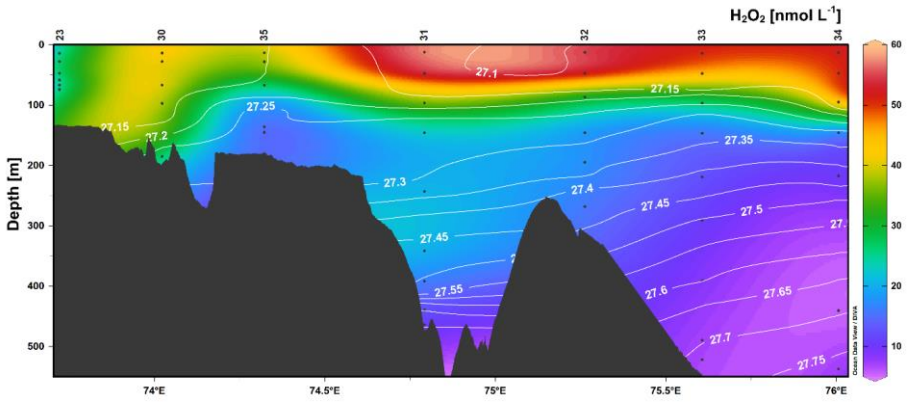

Figure 4. Transect C H_2O_2 concentrations, with neutral density (γ^n; kg m^{-2}) surfaces overlaid (white lines, calculated from continuous CTD data). Black dots represent sample locations. Station numbers for TMR deployments are shown above the top axis.

3.2.2. Heard and McDonald Islands

Surface concentrations of H_2O_2 around HIMI were highest at stations most likely affected by open ocean waters flowing along the western edge of the plateau and associated with the Fawn Trough Current: station 16, northwest of McDonald, and stations 20 and 21 south of HIMI. All other stations had homogeneous H_2O_2 profiles, with surface concentrations ranging between 13.5 – 31.0 nmol L^{-1} at McDonald Islands and 20.8 – 29.3 nmol L^{-1} at Heard Island (Figure 3).

3.2.1. Reference Station

The mean surface H_2O_2 concentration in the upper 100 m was 30.6 ± 6.1 nmol L^{-1}, n = 4. Hydrogen peroxide rapidly decreased with depth down to 200 m (the mixed layer depth) and then decreased more gradually to 1000 m (Figure 3).

.

4. Discussion

Dissolved Fe(II) concentrations as high as 0.57 nmol L^{-1} were measured in waters north of Heard Island and 1.01 nmol L^{-1} to the east of McDonald Islands. These concentrations are higher than most existing DFe(II) measurements in open Southern Ocean surface waters, which are generally below 0.03 nmol L^{-1} (Bowie et al., 2002; Sarthou et al., 2011). Peroxide concentrations around HIMI (13.5 – 31.0 nmol L^{-1}) were consistent with the nearest Southern Ocean observations taken ~700 km west of the Kerguelen Plateau (4.9 – 20.2 nmol L^{-1}; Sarthou et al., 1997).

Sources of DFe(II) near HIMI may include benthic fluxes from anoxic and sub-oxic sediments (Lohan and Bruland, 2008), hydrothermal fluids (Holmes et al., 2017), glacial runoff (Raiswell et al., 2018) and atmospheric deposition of aerosols (Croot and Heller,

2012). Additional production mechanisms of DFe(II) in the surface ocean include photochemistry, through the breakdown and reduction of Fe(III)-ligand complexes (Rijkenberg et al., 2005) and biological production, through bioreduction of Fe(III)-ligand complexes (Maldonado and Price, 1999), grazing (Gobler et al., 1997) or viral lysis of cells (Hutchins and Bruland, 1994). We now discuss each of these sources in relation to data collected during the HEOBI voyage in order to identify potential influences on the elevated Fe(II) concentrations observed in the region.

4.1. Glacial runoff

At Heard Island, glacial runoff appears to be the most important source of Fe(II), with evidence suggesting that the elevated DFe(II) signal at station 24 originates from Heard Island glacial meltwaters. Comparing DFe(II) concentrations with salinity at stations north of Heard Island suspected of being influenced by glacial processes (stations 24, 23 and 36 – 40) shows a significant inverse correlation ($R^2 = 0.57$, $P < 0.01$; Figure 5). Samples taken at the station in front of Downes and Ealey marine terminating glaciers (station 24) are distinct from the other Heard Island samples, with higher DFe(II) concentrations (mean 0.53 nmol L^{-1}) compared to nearby stations (mean DFe(II) 0.18 nmol L^{-1} at stations 36 – 40).

The percentage of DFe(II) relative to DFe(total) can indicate the presence of a strong Fe(II) source (e.g. Sedwick et al., 2015). Dissolved Fe(II) concentrations at the Heard Island station closest to Downes and Ealey glaciers (station 24) were an order of magnitude higher than those observed at the reference station (below detection – 0.05 nmol L^{-1} range in the upper 100 m), i.e. regional open ocean conditions (Figure 3). Mean DFe(II) percentage over the water column at station 24 was also high at 25% (Figure 6). This enrichment in DFe(II) suggests that there was a strong DFe(II) source adjacent to the glacial outflow, which supported the elevated concentrations observed to the north of Heard Island in well oxygenated waters (median 328 µmol L^{-1} O_2).

High DFe(II) (0.44 nmol L^{-1}) and DFe (1.88 nmol L^{-1}) concentrations were also observed in the upper 30 m downstream to the east (7 km) of station 24 (station 23, Figure 3), where targeted sampling was undertaken based on a large acoustic plume (Spain et al., 2019). This area was later revisited and sampled in a crosshair pattern (stations 36 – 40) in an attempt to delineate the signal source. However, these crosshair stations yielded lower DFe(II) and DFe concentrations (mean 0.15 ± 0.1 and 1.53 ± 0.19 nmol L^{-1}, n = 21, respectively) compared to the elevated samples observed previously (station 23) or further to the west, towards the glacier terminus (station 24). This discrepancy in observed DFe(II) concentrations between station 23 and the crosshair stations (36 – 40), which were sampled at almost the same location only 7 days later, attests to the dynamic circulation of the region. The two samples in the upper 30 m of station 23 were also associated with water that was lower in salinity and higher in DFe(II) than revisited crosshair stations 36 – 40, but slightly lower in DFe(II) than station 24 samples. This is likely laterally advected, glacially influenced surface water that has diluted and/or from which DFe(II) has oxidised/precipitated with distance from the Heard Island source. Indeed, particle laden waters advecting away from Heard Island are visible in satellite imagery of the region (van der Merwe et al., 2019). Furthermore, previous studies have shown that glacial erosion and melting results in runoff enriched with DFe (Raiswell et al., 2018). 'Dissolved' iron may also include particles <0.4 µm, including Fe(II)-enriched nanoparticles (Hawkings et al., 2018; Shoenfelt et al., 2017), from which DFe(II) may be released and stabilised by ligands (Hawkings et al., 2018; Hopwood et al., 2014) or may be accessible in the solid phase (Shoenfelt et al., 2017).

Suspended particulate analysis from the HEOBI voyage provides additional evidence that waters to the north of Heard Island are influenced by glacial runoff (van der Merwe et al., 2019). Immediately adjacent to the large marine terminating glacier on the north of Heard Island, suspended particles were found to be highly labile, with higher proportions of Fe

oxyhydroxide nanoparticles, in contrast to less-labile, lithogenic Fe bearing mineral particles observed at McDonald Islands (van der Merwe et al., 2019). Iron oxyhydroxide nanoparticles can be formed from DFe(II) and can produce DFe(II) through dissolution enhanced by photochemical reduction and digestion by protozoan grazers (Barbeau et al., 1996). Ascertaining the exact mechanism of the glacial Fe(II) production was outside the scope of this study. However, glacial flour observed at station 24 (van der Merwe et al., 2019) and high concentrations of non-algal particles (Wojtasiewicz et al., 2019) seems to indicate that Fe(II) production was likely due to physical weathering of underlaying basalt by the glacier (van der Merwe et al., 2019). High silica concentrations observed at this site (van der Merwe et al., 2019) may also indicate that this physical weathering resulted in mobilisation of Fe(II) silicates, as has been demonstrated in previous studies (Shoenfelt et al., 2019). These could be important mechanisms in maintaining the observed DFe(II) and DFe enrichment at Heard Island.

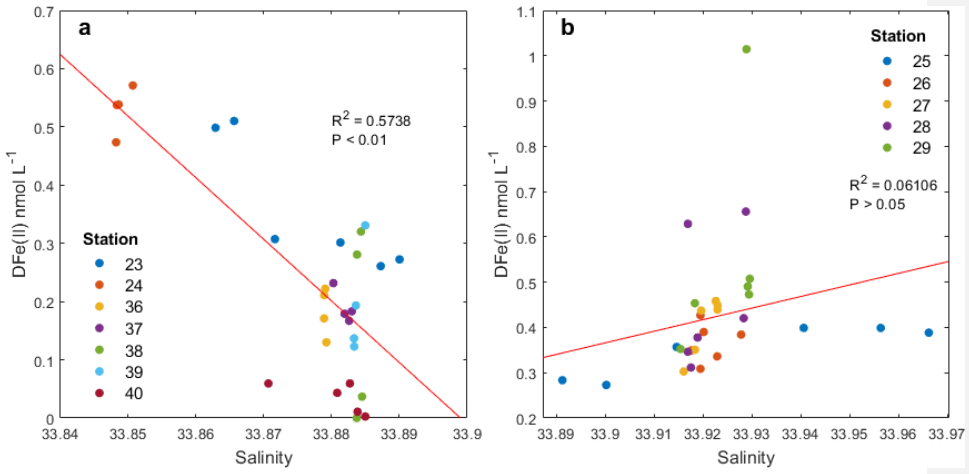

Figure 5. DFe(II) versus Salinity at **a.** Heard Island station 24 and crosshair stations 23, 36 – 40 and **b.** McDonald Islands crosshair stations 25 – 29. Station numbers are annotated.

4.2. Hydrothermal sources

At McDonald Islands, hydrothermal inputs appear to be the most important source of Fe(II), with evidence suggesting that the elevated DFe(II) signal at stations 28 and 29 originated from diffuse hydrothermal sources. Numerous acoustic flare signals detected by ship-board echosounder and footage of bubbles emanating from the seafloor (Figure 7) at several locations around HIMI, were clues that hydrothermal vents were present in the region. The presence of localised DFe(II) maxima (Figure 3), elevated DFe(II) to DFe(total) ratios (Figure 6), sharp DFe(II) spikes in the water column (Figure 8), along with observations of excess ^{3}He with clear hydrothermal origins (Lupton et al., 2017), indicate that shallow water (<200 m) hydrothermalism was a likely source of DFe(II) at stations west of McDonald Islands.

The first clue that hydrothermalism may be a dominant source of DFe(II) at McDonald Islands is the presence of localised elevated DFe(II) maxima. Five stations (25 – 29) were sampled to the east of McDonald Islands in a 'crosshair' pattern (Figure 1). These sampling locations were selected in an attempt to further delineate elevated DFe concentrations detected at a previous station (station 12; Holmes et al., 2019) and where strong acoustic flare signals were observed (Spain et al., 2019). Mean DFe(II) concentrations at the McDonald crosshair stations were significantly higher (t-test, $P < 0.01$; Figure 8c) than the Heard crosshair stations, and exhibited pronounced spikes in DFe(II) at various depths at two of the stations.

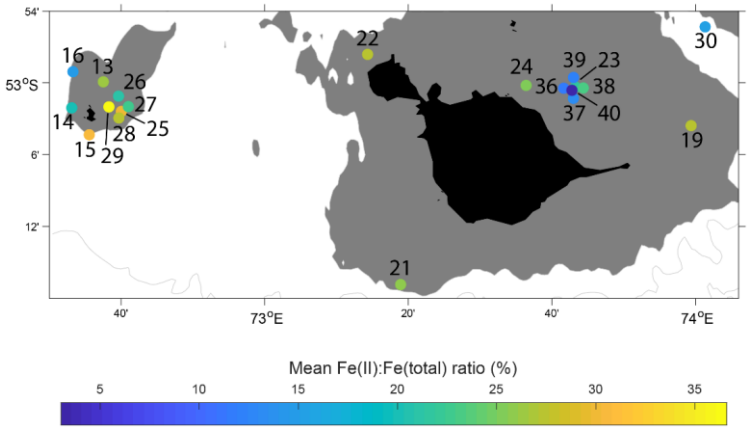

Figure 6. Mean Fe(II) to Fe(total) percentage over the water column for each station near Heard and McDonald Islands. Note that station 20 is omitted as data are at detection limits, giving a falsely high ratio.

The station closest to McDonald Islands at the western side of the crosshair (station 29), had the greatest DFe(II) concentration and DFe(II):DFe(total) percentage observed during HEOBI (1.01 nmol L^{-1} and 37%, respectively; Figure 6). The next highest maximum DFe(II) concentration (0.66 nmol L^{-1}) was observed at the southernmost crosshair station (station 28). These stations were separated by a distance of 780 m and ~1.5 hours between sampling. These spikes in maximum DFe(II) concentrations, located at varying depths, were unusual compared to other stations around HIMI (Figure 3). The other three stations of the crosshair (25, 26 and 27; 630 m east-southeast, 730 m northeast and 1040 m east from station 29, respectively) had lower overall DFe(II) concentrations and were more homogeneous over the water column (0.27 – 0.40, 0.31 – 0.43 and 0.30 – 0.46 nmol L^{-1}, respectively). The existence of profiles with pronounced spikes in DFe(II) concentrations and profiles with homogenous DFe(II) among the closely spaced crosshair stations may attest to the turbulent mixing and rapidly oxidising conditions in the region and indicates that the DFe(II) originates from point source(s) such as a vent or patch, rather than a larger area of the seafloor, such as might be expected from benthic flux.

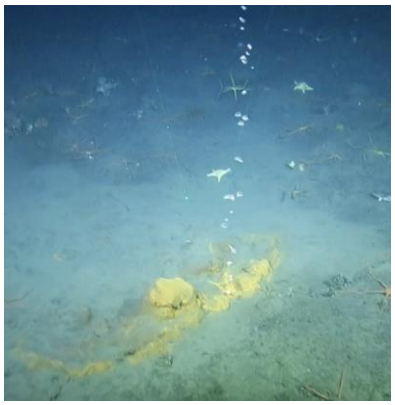

Figure 7. Bubbles rising from the seafloor at a site NE of Heard Island, captured using deep tow camera during the HEOBI voyage. Though plumes were detected using echosounder around both islands, no bubble plumes were captured on camera near McDonald Islands. Photo courtesy of the Marine National Facility, CSIRO.

The presence of DFe(II) peaks at various depths in the water column at the two stations (28, 29) with the most elevated DFe(II) could indicate that TMR casts intercepted point source plumes as the ship and/or rising plumes moved laterally with currents (e.g. Bennett et al., 2009). Due to the turbulent nature of waters surrounding HIMI, and the point source nature of the observed elevated DFe(II) concentrations at the McDonald Islands crosshair stations, it is unlikely that a TMR cast would stay within a plume for the duration of the cast (~1 hour). A DFe(II) point source would also make sampling directly above the source challenging without a remotely operated vehicle.

Numerous observations via deep tow camera of bubbles emitted from seafloor vents scattered around the entire region during the HEOBI voyage (Figure 7) and recent δ^3He anomaly data (an unequivocal tracer of hydrothermalism; Lupton et al., 2017) add further evidence that diffuse hydrothermal venting is a likely source of DFe(II) at McDonald Islands. The greatest δ^3He enrichment (10.1%) in the region was observed in the vicinity of the crosshair station group near McDonald Islands, compared to 1.7% close to station 37, near the northeast of Heard Island (Lupton et al., 2017). Acoustic flares, detected by the shipboard echosounder, were observed at both Heard and McDonald Islands (Spain et al., 2019). This may suggest

Moved (insertion) [1]

that while there were stronger glacial sources of DFe(II) at Heard Island, hydrothermalism may have contributed to elevated background concentrations observed around both islands, along with sedimentary and other sources (discussed below).

4.3. Sedimentary sources

Sediments are another potential DFe(II) source in the HIMI region. Relatively high particle backscattering was observed around HIMI (Wojtasiewicz et al., 2019) and wind-driven mixing events often reached the seafloor around HIMI during the voyage resulting in a well-mixed water column homogeneous in properties such as temperature and salinity (R. Robertson, pers. comm.). This mixing could disturb upper oxidising sediment layers, resuspend sediments and potentially facilitate the escape of Fe(II) from underlying anoxic sediments (e.g. Elrod et al., 2004). However, with the exception of stations 15 and 21, no obvious maximum in DFe(II) was observed near the seafloor as would be expected if sedimentary sources dominated (Figure 3). Sediments on continental shelves have been identified as strong DFe(II) sources, especially in the presence of hypoxic bottom waters (Lohan and Bruland, 2008). In the presence of oxygenated bottom waters, the upper layer of sediment tends to form an oxidising barrier, meaning relatively little DFe(II) can penetrate into the overlying water column (Homoky et al., 2016). However, an example of benthic flux of Fe(II) to oxygenated bottom waters has been observed in a region of hydrothermal activity in the Bransfield Straight, Southern Ocean (Aquilina et al., 2014). This flux was attributed to infaunal tubeworms, the remains of which provided conduits for subsurface fluid to bypass the upper sediment layer (Aquilina et al., 2014). Though there was no biologically focused sampling program during the HEOBI voyage, bioturbation of surface sediments is likely, due to the shallow bathymetry and biological productivity in the region – including a rich diversity of benthic species (Améziane et al., 2011). However, If the source of elevated DFe(II) at the McDonald crosshair stations was sedimentary in origin, we would expect to

see an increase in concentrations towards the seafloor over a larger area (Lohan and Bruland, 2008), which was not observed during HEOBI.

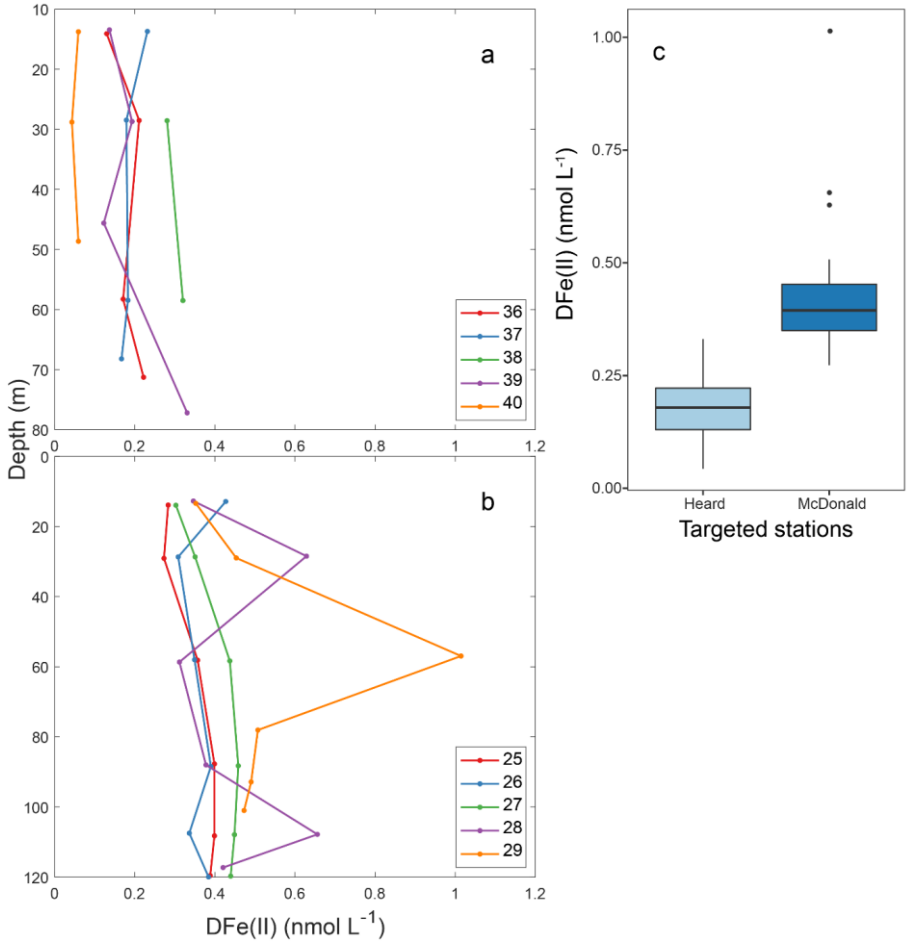

Figure 8. DFe(II) versus depth at **a.** Heard Island crosshair stations (36 – 40) and **b.** McDonald Islands crosshair stations 25 – 29. Station numbers are annotated. Note that due to analytical constraints, replicate measurements were unavailable for some samples. Therefore, given the well mixed nature of the water around both islands, data from each of the crosshair sites has been summarised in **c.** boxplots. The bottom and top limits of the boxes represent the 25th and 75th percentiles, respectively. The horizontal line within the box represents the median. The lower and upper whiskers extend from the 25th and 75th percentiles to the lowest and highest values within the interquartile range, respectively. Solid circles represent outlying values. Data lower than detection limits have been excluded.

Moved up [1]: compared to 1.7% close to station 37, near the northeast of Heard Island (Lupton et al., 2017). Acoustic flares, detected by the shipboard echosounder, were observed at both Heard and McDonald Islands (Spain et al., 2019). This may suggest that while there were stronger glacial sources of DFe(II) at Heard Island, hydrothermalism may have contributed to elevated background concentrations observed around both islands, along with sedimentary and other sources (discussed below).

4.4. Other DFe(II) sources and sinks

Photochemical processes, H_2O_2 and O_2 concentrations, atmospheric deposition of wet and dry aerosols, biological processes and changes in seawater pH all represented potential sources and sinks in the HIMI region during HEOBI. Production of Fe(II) through photochemical processes did not appear to be the strongest influence of DFe(II) concentrations around HIMI, as comparison of shipboard surface photosynthetically active radiation (PAR) observations with surface DFe(II) concentrations showed no correlation (Figure S1). Surface H_2O_2 concentrations also showed no correlation with PAR (Figure S1); however, concentrations in surface waters were correlated with distance from land ($R^2 = 0.70$, $P < 0.01$), with greatest surface H_2O_2 observed at stations furthest from HIMI (i.e. stations 9 and 10 on the central northern plateau and 30 – 35 on transect C; Figure 3, 4). These stations were deeper and could thus form a stratified surface mixed layer, allowing H_2O_2 to accumulate above the pycnocline. Surface H_2O_2 showed a weak relationship ($R^2 = 0.18$, $n = 26$) with surface DFe(II) concentrations (Figure S2). The low H_2O_2 concentrations and lack of correlation between DFe(II) and either H_2O_2, O_2, or PAR around HIMI suggests that on-plateau DFe(II) distributions are predominantly governed by strong local DFe(II) sources.

Atmospheric deposition did not appear to be a major source of dissolved or particulate Fe during HEOBI, and therefore not a major source of DFe(II), as DFe(II) represents a fraction of total Fe. Wet deposition of DFe(II) and H_2O_2 was not apparent (Figure S1), possibly because of the minimal precipitation during HEOBI. The mean aerosol soluble Fe observed during HEOBI (0.30 ± 0.12 ng m^{-3}; $n = 13$, M. M. G. Perron, pers. comm.) was on the same order as values found near Kerguelen Island to the north (0.29 ± 0.14 ng m^{-3}; Blain et al., 2008), which were not deemed to be a significant source of DFe to that region (Blain et al., 2008). These values also fall in the range of baseline Southern Ocean aerosol soluble Fe (0.01 – 0.3 ng m^{-3}; Winton et al., 2015), where surface concentrations of DFe(II) are reported to

range from below detection to 30 pmol L^{-1}. Thus, we can assume that the contribution of dry deposition aerosols to DFe(II) observations in the water column is probably minor.

Biological production by processes such as viral lysis of cells (Gobler et al., 1997) and grazing (Hutchins and Bruland, 1994) likely contributed to background DFe(II) concentrations in waters around HIMI. While no direct observations were taken to enable an estimate of the biological production of DFe(II) during HEOBI, it can be inferred from our observations that biological production was not the greatest source of elevated DFe(II) observed near Heard or McDonald Islands. Indeed, Wojtasiewicz et al. (2019) showed that during HEOBI phytoplankton communities around HIMI were limited by low light availability due to deep mixing and shading by re-suspended sediment particles and augmented by dilution with surrounding low chlorophyll waters of the Antarctic Circumpolar Current.

In addition, pH and temperature conditions should be considered in relation to Fe(II) half-life in the HIMI region. Low temperatures, such as those found in waters around HIMI, extend Fe(II) half-life in high-latitude waters by slowing oxidation reactions ((Millero et al., 1987; Millero and Sotolongo, 1989)). Our Fe(II) half-life calculations agree with previous studies (e.g. Millero et al., 1987) showing that pH has a significant impact on Fe(II) half-life (Figure S3). Using in-situ observations of variables required in the equations and changing pH in steps of 0.1 units shows the strong dependence of Fe(II) half-life on pH (Figure S3). These results indicate that input of low pH fluids from diffuse hydrothermal sources could dramatically impact Fe(II) speciation and half-life close to vent sources, as has been observed previously at other diffuse hydrothermal vent sites (e.g. McCarthy et al., 2005).

It is likely that aerosol deposition, biological production and photochemical processes, coupled with low water temperature and possibly localised lower pH in areas of the region,

contributed to the overall elevated DFe(II) concentrations observed at stations in the HIMI region.

4.5. Fe(II) transport

Using current velocities observed during HEOBI (R. Robertson, pers. comm.) and previous voyages (Park et al., 2008), and our modelled Fe(II) half-lives, a rough estimate of the distance Fe(II) might travel from HIMI can be calculated. Modelled half-lives ranged from 30 minutes to 172 hours. Current velocities over the plateau were slow (~6 cm s^{-1}), while currents to the east of Heard Island were stronger (~40 cm s^{-1}), in agreement with previous observations (Park et al., 2008). Both currents over the plateau and to the east of Heard Island flowed in a northerly direction. Using these figures, the distance Fe(II) could theoretically travel in one half-life over the plateau ranged from ~100 m to ~37 km. If Fe(II) reached the stronger currents to the east of Heard Island, in one half-life Fe(II) could theoretically travel between ~700 m and ~250 km. Considering that the greatest Fe(II) concentration observed at HIMI (~1 nmol L^{-1}) will take approximately 5 half-lives to reach surface Southern Ocean background concentrations (~0.03 nmol L^{-1}; Sarthou et al., 2011), it is plausible that Fe(II) from hydrothermal and glacial sources at HIMI could travel the distances required to fertilise the phytoplankton plume that forms over the plateau annually. This may have implications for future Fe supply to the northern plateau, since under warming climate conditions, melting glacial waters may increase, potentially increasing the supply of DFe(II), and could then rapidly decrease once glaciers have melted.

5. Conclusion

We show that the strongest sources of DFe(II) differ between adjacent, volcanically active Heard and McDonald Islands. Maximum DFe(II) concentrations and varying mid-depth maxima in the water column at adjacent, targeted stations at McDonald Islands suggest that

hydrothermalism is the strongest DFe(II) source. At Heard Island, the strongest DFe(II) source correlates with low salinity waters and is near a marine-terminating glacier, suggesting that glacial meltwater (and possibly associated glacial flour) is the major source of DFe(II). Revisited stations to the east of the strongest signal showed a temporary freshwater and elevated DFe(II) signal, which suggests that glacially fertilised waters may be transported offshore from Heard Island. These results are in agreement with preliminary δ^3He (Lupton et al., 2017) and particulate Fe data (van der Merwe et al., 2019) also collected during the HEOBI voyage.

Peroxide and PAR data shows that neither H_2O_2 or PAR correlate with DFe(II) concentrations around HIMI, suggesting that on-plateau DFe(II) concentrations are predominantly governed by strong local DFe(II) sources. Preliminary aerosol data collected during the HEOBI voyage confirms that soluble aerosol concentrations were low. The homogenous nature of most DFe(II) and H_2O_2 profiles around HIMI highlights the strong mixing regime in the region but obscures some features that would allow direct attribution to a source. Further research is necessary to determine exact mechanisms of decay and/or consumption of DFe(II) in the water column. In addition to the strong sources from hydrothermal and glacial inputs identified in this study, the overall elevated concentrations of DFe(II) around HIMI are likely to be an accumulation of multiple sources (sedimentary resuspension, surface irradiance, biological production and atmospheric deposition), in addition to opposing controls on DFe(II) half-life from low temperature, highly oxygenated waters and potentially lower pH, which have all been homogenised in the well mixed water column. The elevated concentrations of DFe(II) around HIMI, a highly labile and bioavailable form of Fe, may increase Fe availability for biota in the region. High DFe(II) concentrations may also indicate slower oxidation kinetics in the region, which has

574 implications for transport of Fe away from the islands to the broader northern Kerguelen
575 Plateau where the annual plankton bloom is strongest.

576 **6. Acknowledgements**

577 The authors would like to thank Elizabeth Shoenfelt Troein and an anonymous reviewer for
578 their detailed and constructive comments, which greatly improved this manuscript. We thank
579 Rob Middag (University of Otago, New Zealand) for supplying the FIA-CL instrument that
580 was used to analyse H_2O_2 samples during the voyage, Manon Tonnard (Laboratoire des
581 sciences de l'Environnement MARin: LEMAR) and Lavenia Ratnarajah (Antarctic Climate
582 and Ecosystems Cooperative Research Centre and Institute for Marine and Antarctic Studies:
583 ACECRC, IMAS) for their assistance in collecting and filtering samples on the HEOBI
584 voyage. We would like to thank Mark Rayner and Kendall Sherrin for their excellent oxygen
585 analyses. We also thank the captain, officers and crew of the RV Investigator (HEOBI
586 voyage) and Chief Scientist Mike Coffin for their support during the 53-day expedition. We
587 wish to acknowledge the Australian Research Council (DP150100345 and LE0989539), the
588 Australian Antarctic Science Program (AAS4338) and the Australian Government
589 Cooperative Research Centres Program through the Antarctic Climate and Ecosystems CRC,
590 who provided project funding and PhD scholarship support. Dissolved Fe(II) and H_2O_2 data
591 are publicly available online in the CSIRO data repository
592 (https://doi.org/10.25919/5eeff98b11d39).

593 **7. References**

594 Améziane, N., Eléaume, M., Hemery, L.G., Monniot, F., Hemery, A., Hautecoeur, M., Dettaï,
595 A., 2011. Biodiversity of the benthos off Kerguelen Islands : overview and perspectives.
596 Kerguelen Plateau Mar. Ecosyst. Fish. 157–167.

597 Aquilina, A., Homoky, W.B., Hawkes, J.A., Lyons, T.W., Mills, R.A., 2014. Hydrothermal

598 sediments are a source of water column Fe and Mn in the Bransfield Strait, Antarctica.
599 Geochim. Cosmochim. Acta 137, 64–80. doi:10.1016/j.gca.2014.04.003

600 Barbeau, K., Moffett, J.W., Caron, D.A., Croot, P.L., Erdner, D.L., 1996. Role of protozoan
601 grazing in relieving iron limitation of phytoplankton. Nature 380, 61–64.
602 doi:10.1038/380061a0

603 Bennett, S.A., Rouxel, O., Schmidt, K., Garbe-Schönberg, D., Statham, P.J., German, C.R.,
604 2009. Iron isotope fractionation in a buoyant hydrothermal plume, 5°S Mid-Atlantic
605 Ridge. Geochim. Cosmochim. Acta 73, 5619–5634. doi:10.1016/j.gca.2009.06.027

606 Blain, S., Sarthou, G., Laan, P., 2008. Distribution of dissolved iron during the natural iron-
607 fertilization experiment KEOPS (Kerguelen Plateau, Southern Ocean). Deep Sea Res.
608 Part II Top. Stud. Oceanogr. 55, 594–605. doi:10.1016/j.dsr2.2007.12.028

609 Bowie, A.R., Achterberg, E.P., Sedwick, P.N., Ussher, S., Worsfold, P.J., 2002. Real-Time
610 Monitoring of Picomolar Concentrations of Iron (II) in Marine Waters Using Automated
611 Flow Instrumentation. Environ. Sci. Technol. 36, 4600–4607. doi:10.1021/es020045v

612 Bowie, A.R., Achterberg, E.P., Ussher, S., Worsfold, P.J., 2005. Design of an automated flow
613 injection-chemiluminescence instrument incorporating a miniature photomultiplier tube
614 for monitoring picomolar concentrations of iron in seawater. J. Autom. Methods Manag.
615 Chem. 2005, 37–43. doi:10.1155/JAMMC.2005.37

616 Boyd, P.W., Ellwood, M.J., 2010. The biogeochemical cycle of iron in the ocean. Nat.
617 Geosci. doi:10.1038/ngeo964

618 Boyd, P.W., Jickells, T., Law, C.S., Blain, S., Boyle, E. a, Buesseler, K.O., Coale, K.H.,
619 Cullen, J.J., de Baar, H.J.W., Follows, M., Harvey, M., Lancelot, C., Levasseur, M.,
620 Owens, N.P.J., Pollard, R., Rivkin, R.B., Sarmiento, J., Schoemann, V., Smetacek, V.,

621 Takeda, S., Tsuda, a, Turner, S., Watson, a J., 2007. Mesoscale iron enrichment
622 experiments 1993-2005: synthesis and future directions. Science 315, 612–7.
623 doi:10.1126/science.1131669

624 Cohan, D.S., Schultz, M.G., Jacob, D.J., Heikes, B.G., Blake, D.R., 1999. Convective
625 injection and photochemical decay of peroxides in the tropical upper troposphere:
626 Methyl iodide as a tracer of marine convection. J. Geophys. Res. Atmos. 104, 5717–
627 5724. doi:10.1029/98JD01963

628 Croot, P.L., Heller, M.I., 2012. The importance of kinetics and redox in the biogeochemical
629 cycling of iron in the surface ocean. Front. Microbiol. 3, 219.
630 doi:10.3389/fmicb.2012.00219

631 Croot, P.L., Streu, P., Peeken, I., Lochte, K., Baker, A.R., 2004. Influence of the ITCZ on
632 H2O2 in near surface waters in the equatorial Atlantic Ocean. Geophys. Res. Lett. 31,
633 1–4. doi:10.1029/2004GL020154

634 Cutter, G., Andersson, P., Codispoti, L., Croot, P., Francois, R., Lohan, M., Obata, H.,
635 Rutgers, M., 2014. Sampling and Sample-handling Protocols for GEOTRACES Cruises.

636 Elrod, V. a., Berelson, W.M., Coale, K.H., Johnson, K.S., 2004. The flux of iron from
637 continental shelf sediments: A missing source for global budgets. Geophys. Res. Lett.
638 31, n/a-n/a. doi:10.1029/2004GL020216

639 Gobler, C.J., Hutchins, D.A., Fisher, N.S., Cosper, E.M., Sañudo-Wilhelmy, S.A., 1997. Release
640 and bioavailability of C, N, P, Se, and Fe following viral lysis of a marine chrysophyte.
641 Limnol. Oceanogr. 42, 1492–1504. doi:10.4319/lo.1997.42.7.1492

642 González-Dávila, M., Santana-Casiano, J.M., Millero, F.J., 2006. Competition between O2 and
643 H2O2 in the oxidation of Fe(II) in natural waters. J. Solution Chem. 35, 95–111.

644 doi:10.1007/s10953-006-8942-3

645 Hawkes, J.J.A., Connelly, D.P., Rijkenberg, M.J.A., Achterberg, E.P., 2014. The importance
646 of shallow hydrothermal island arc systems in ocean biogeochemistry. Geophys. Res.
647 Lett. 41, 942–947. doi:10.1002/2013GL058817

648 Hawkings, J.R., Benning, L.G., Raiswell, R., Kaulich, B., Araki, T., Abyaneh, M., Stockdale,
649 A., Koch-müller, M., Wadham, J.L., Tranter, M., 2018. Biolabile ferrous iron bearing
650 nanoparticles in glacial sediments. Earth Planet. Sci. Lett. 493, 92–101.
651 doi:10.1016/j.epsl.2018.04.022

652 Holmes, T.M., Chase, Z., Van Der Merwe, P., Townsend, A.T., Bowie, A.R., 2017.
653 Detection, dispersal and biogeochemical contribution of hydrothermal iron in the ocean.
654 Mar. Freshw. Res. 68, 2184–2204. doi:10.1071/MF16335

655 Holmes, T.M., Wuttig, K., Chase, Z., van der Merwe, P., Townsend, A.T., Schallenberg, C.,
656 Tonnard, M., Bowie, A.R., 2019. Iron availability influences nutrient drawdown in the
657 Heard and McDonald Islands region, Southern Ocean. Mar. Chem. 211, 1–14.
658 doi:10.1016/j.marchem.2019.03.002

659 Homoky, W.B., Weber, T., Berelson, W.M., Conway, T.M., Henderson, G.M., van Hulten,
660 M., Jeandel, C., Severmann, S., Tagliabue, A., 2016. Quantifying trace element and
661 isotope fluxes at the ocean–sediment boundary: a review, Philosophical Transactions of
662 the Royal Society A: Mathematical, Physical and Engineering Sciences.
663 doi:10.1098/rsta.2016.0246

664 Hopwood, M.J., Statham, P.J., Tranter, M., Wadham, J.L., 2014. Glacial flours as a potential
665 source of Fe(II) and Fe(III) to polar waters. Biogeochemistry 118, 443–452.
666 doi:10.1007/s10533-013-9945-y

667 Hutchins, D.A., Bruland, K.W., 1994. Grazer-mediated regeneration and assimilation of Fe, Zn
668 and Mn from planktonic prey. Mar. Ecol. Prog. Ser. 110, 259–270.
669 doi:10.3354/meps110259

670 Hwang, H., Dasgupta, P.K., 1985. Thermodynamics of the hydrogen peroxide-water system.
671 Environ. Sci. Technol. 19, 255–258. doi:10.1021/es00133a006

672 Lohan, M.C., Bruland, K.W., 2008. Elevated Fe(II) and dissolved Fe in hypoxic shelf waters
673 off Oregon and Washington: An enhanced source of iron to coastal upwelling regimes.
674 Environ. Sci. Technol. 42, 6462–6468. doi:10.1021/es800144j

675 Lupton, J.E., Arculus, R.J., Coffin, M., Bradney, A., Baumberger, T., Wilkinson, C., 2017.
676 Hydrothermal venting on the flanks of Heard and McDonald islands, southern Indian
677 Ocean, in: AGU Fall Meeting Abstracts. p. V51F–0435.

678 Maldonado, M.T., Price, N.M., 1999. Utilization of iron bound to strong organic ligands by
679 plankton communities in the subarctic Pacific Ocean. Deep. Res. Part II Top. Stud.
680 Oceanogr. 46, 2447–2473. doi:10.1016/S0967-0645(99)00071-5

681 Martin, J.H., Gordon, R.M., Fitzwater, S.E., 1990. Iron in Antarctic waters. Nature 345, 156–
682 158. doi:10.1038/345156a0

683 McCarthy, K.T., Pichler, T., Price, R.E., 2005. Geochemistry of Champagne Hot Springs
684 shallow hydrothermal vent field and associated sediments, Dominica, Lesser Antilles.
685 Chem. Geol. 224, 55–68. doi:10.1016/j.chemgeo.2005.07.014

686 Millero, F.J., Sotolongo, S., 1989. The oxidation of Fe(II) with H2O2 in seawater. Geochim.
687 Cosmochim. Acta 53, 1867–1873. doi:10.1016/0016-7037(89)90307-4

688 Millero, F.J., Sotolongo, S., Izaguirre, M., 1987. The oxidation kinetics of Fe(II) in seawater.
689 Geochim. Cosmochim. Acta 51, 793–801. doi:10.1016/0016-7037(87)90093-7

690 Moore, C.M., Mills, M.M., Achterberg, E.P., Geider, R.J., LaRoche, J., Lucas, M.I.,
691 McDonagh, E.L., Pan, X., Poulton, A.J., Rijkenberg, M.J. a., Suggett, D.J., Ussher, S.J.,
692 Woodward, E.M.S., 2009. Large-scale distribution of Atlantic nitrogen fixation
693 controlled by iron availability. Nat. Geosci. 2, 867–871. doi:10.1038/ngeo667

694 Palenik, B., Morel, F.M.M., 1988. Dark production of H2O2 in the Sargasso Sea. Limnol.
695 Oceanogr. 33, 1606–1611. doi:10.4319/lo.1988.33.6part2.1606

696 Park, Y.Y.-H., Durand, I., Kestenare, E., Rougier, G., Zhou, M., d'Ovidio, F., Cotté, C., Lee,
697 J.-H., 2014. Polar Front around the Kerguelen Islands: An up-to-date determination and
698 associated circulation of surface/subsurface waters. J. Geophys. Res. Ocean. 1–18.
699 doi:10.1002/2014JC010061.Received

700 Park, Y.-H., Roquet, F., Durand, I., Fuda, J.-L., 2008. Large-scale circulation over and around the
701 Northern Kerguelen Plateau. Deep Sea Res. Part II Top. Stud. Oceanogr. 55, 566–581.
702 doi:10.1016/j.dsr2.2007.12.030

703 Raiswell, R., Hawkings, J., Elsenousy, A., Death, R., Tranter, M., Wadham, J., 2018. Iron in
704 Glacial Systems: Speciation, Reactivity, Freezing Behavior, and Alteration During
705 Transport. Front. Earth Sci. 6. doi:10.3389/feart.2018.00222

706 Rijkenberg, M.J.A., Fischer, A.C., Kroon, J.J., Gerringa, L.J.A., Timmermans, K.R.,
707 Wolterbeek, H.T., De Baar, H.J.W., 2005. The influence of UV irradiation on the
708 photoreduction of iron in the Southern Ocean. Mar. Chem. 93, 119–129.
709 doi:10.1016/j.marchem.2004.03.021

710 Santana-Casiano, J.M., González-Dávila, M., Millero, F.J., 2006. The role of Fe(II) species
711 on the oxidation of Fe(II) in natural waters in the presence of O_2 and H_2O_2. Mar. Chem.
712 99, 70–82. doi:10.1016/j.marchem.2005.03.010

Sarthou, G., Bucciarelli, E., Chever, F., Hansard, S.P., González-Dávila, M., Santana-Casiano, J.M., Planchon, F., Speich, S., 2011. Labile Fe(II) concentrations in the Atlantic sector of the Southern Ocean along a transect from the subtropical domain to the Weddell Sea Gyre. Biogeosciences 8, 2461–2479. doi:10.5194/bg-8-2461-2011

Sarthou, G., Jeandel, C., Brisset, L., Amouroux, D., Besson, T., Donard, O.F.X., 1997. Fe and H2O2 distributions in the upper water column in the Indian sector of the Southern Ocean. Earth Planet. Sci. Lett. 147, 83–92. doi:10.1016/S0012-821X(97)00004-6

Sedwick, P.., Sohst, B.M., Ussher, S.J., Bowie, A.R., 2015. A zonal picture of the water column distribution of dissolved iron(II) during the U.S. GEOTRACES North Atlantic transect cruise (GEOTRACES GA03). Deep Sea Res. Part II Top. Stud. Oceanogr. 116, 166–175. doi:10.1016/j.dsr2.2014.11.004

Shaked, Y., Kustka, A.B., Morel, M.M., 2005. A general kinetic model for iron acquisition by eukaryotic phytoplankton. Limnol. Oceanogr. 50, 872–882.

Shoenfelt, E.M., Sun, J., Winckler, G., Kaplan, M.R., Borunda, A.L., Farrell, K.R., Moreno, P.I., Gaiero, D.M., Recasens, C., Sambrotto, R.N., Bostick, B.C., 2017. High particulate iron(II) content in glacially sourced dusts enhances productivity of a model diatom. Sci. Adv. 3. doi:10.1126/sciadv.1700314

Shoenfelt, E.M., Winckler, G., Annett, A.L., Hendry, K.R., Bostick, B.C., 2019. Physical Weathering Intensity Controls Bioavailable Primary Iron(II) Silicate Content in Major Global Dust Sources. Geophys. Res. Lett. 46, 10854–10864. doi:10.1029/2019GL084180

Spain, E.A., Johnson, S.C., Hutton, B., Whittaker, J.M., Lucieer, V., Watson, S.J., Fox, J.M., Lupton, J., Arculus, R., Bradney, A., Coffin, M.F., 2019. Shallow seafloor gas emissions near Heard and McDonald Islands on the Kerguelen Plateau, southern Indian Ocean. Earth Sp. Sci. 1–19. doi:10.1029/2019ea000695

Tanhua, T., Olsen, A., Hoppema, M., Jutterström, S., Schirnick, C., van Heuven, S.M.A.C., Velo, A., Lin, X., Kozyr, A., Álvarez, M., Bakker, D.C.E., Brown, P.J., Falck, E., Jeansson, E., Lo Monaco, C., Ólafsson, J., Pérez, F.F., Pierrot, D., Ríos, A.F., Sabine, C.L., Schuster, U., Steinfeldt, R., Stendardo, I., Anderson, L.G., Bates, N., Bellerby, R.G.J., Blindheim, J., Bullister, J.L., Gruber, N., Ishii, M., Johannessen, T., Jones, E.P., Köhler, J., Körtzinger, A., Metzl, N., Murata, A., Musielewicz, S., Omar, A.M., Olsson, K.A., de la Paz, M., Pfeil, B., Rey, F., Rhein, M., Skjelvan, I., Tilbrook, B., Wanninkhof, R., Mintrop, L., Wallace, D.W.R., Key, R.M., 2013. Dissolved inorganic carbon, alkalinity, pH, temperature, salinity, and other variables collected from profile observations using CTD, discrete bottles, and other instruments from October 7, 1977 to March 11, 2006 [WWW Document]. URL https://www.nodc.noaa.gov/OC5/SELECT/dbsearch/dbsearch.html (accessed 7.18.18).

van der Merwe, P., Wuttig, K., Holmes, T., Trull, T.W., Chase, Z., Townsend, A.T., Goemann, K., Bowie, A.R., 2019. High Lability Fe Particles Sourced From Glacial Erosion Can Meet Previously Unaccounted Biological Demand: Heard Island, Southern Ocean. Front. Mar. Sci. 6, 1–20. doi:10.3389/fmars.2019.00332

Watson, S.J., Coffin, M.F., Whittaker, J.M., Lucieer, V., Fox, J.M., Carey, R., Arculus, R.J., Bowie, A.R., Chase, Z., Robertson, R., Martin, T., Cooke, F., 2016. Submarine geology and geomorphology of active Sub-Antarctic volcanoes: Heard and McDonald Islands, in: AGU Fall Meeting Abstracts.

Weller, R., Schrems, O., 1993. H2O2 in the marine troposphere and seawater of the Atlantic Ocean (48°N - 63°S). Geophys. Res. Lett. 20, 125–128. doi:10.1029/93GL00065

Winton, V.H.L., Bowie, A.R., Edwards, R., Keywood, M., Townsend, A.T., van der Merwe, P., Bollhöfer, A., 2015. Fractional iron solubility of atmospheric iron inputs to the

Southern Ocean. Mar. Chem. 177, 20–32. doi:10.1016/j.marchem.2015.06.006

Wojtasiewicz, B., Trull, T.W., Clementson, L., Davies, D.M., Patten, N.L., Schallenberg, C., Hardman-Mountford, N.J., 2019. Factors Controlling the Lack of Phytoplankton Biomass in Naturally Iron Fertilized Waters Near Heard and McDonald Islands in the Southern Ocean. Front. Mar. Sci. 6. doi:10.3389/fmars.2019.00531

Yuan, J., Shiller, A.M., 1999. Determination of subnanomolar levels of hydrogen peroxide in seawater by reagent-injection chemiluminescence detection. Anal. Chem. 71, 1975–1980. doi:10.1021/ac981357c

8. List of Figures

Figure 4. Transect C H_2O_2 concentrations, with neutral density (γ^n; kg m^{-2}) surfaces overlaid (white lines, calculated from continuous CTD data). Black dots represent sample locations. Station numbers for TMR deployments are shown above the top axis.

Figure 5. DFe(II) versus Salinity at **a.** Heard Island station 24 and crosshair stations 23, 36 – 40 and **b.** McDonald Islands crosshair stations 25 – 29. Station numbers are annotated.

Figure 6. Mean Fe(II) to Fe(total) percentage over the water column for each station near Heard and McDonald Islands. Note that station 20 is omitted as data are at detection limits, giving a falsely high ratio.

Figure 7. Bubbles rising from the seafloor at a site NE of Heard Island, captured using deep tow camera during the HEOBI voyage. Though plumes were detected using echosounder around both islands, no bubble plumes were captured on camera near McDonald Islands. Photo courtesy of the Marine National Facility, CSIRO.

Figure 8. DFe(II) versus depth at **a.** Heard Island crosshair stations (36 – 40) and **b.** McDonald Islands crosshair stations 25 – 29. Station numbers are annotated. Note that due to analytical constraints, replicate measurements were unavailable for some samples. Therefore, given the well mixed nature of the water around both islands, data from each of the crosshair sites has been summarised in **c.** boxplots. The bottom and top limits of the boxes represent the 25^{th} and 75^{th} percentiles, respectively. The horizontal line within the box represents the median. The lower and upper whiskers extend from the 25^{th} and 75^{th} percentiles to the lowest and highest values within the interquartile range, respectively. Solid circles represent outlying values. Data lower than detection limits have been excluded.

9. Supporting information

9.1. Figures

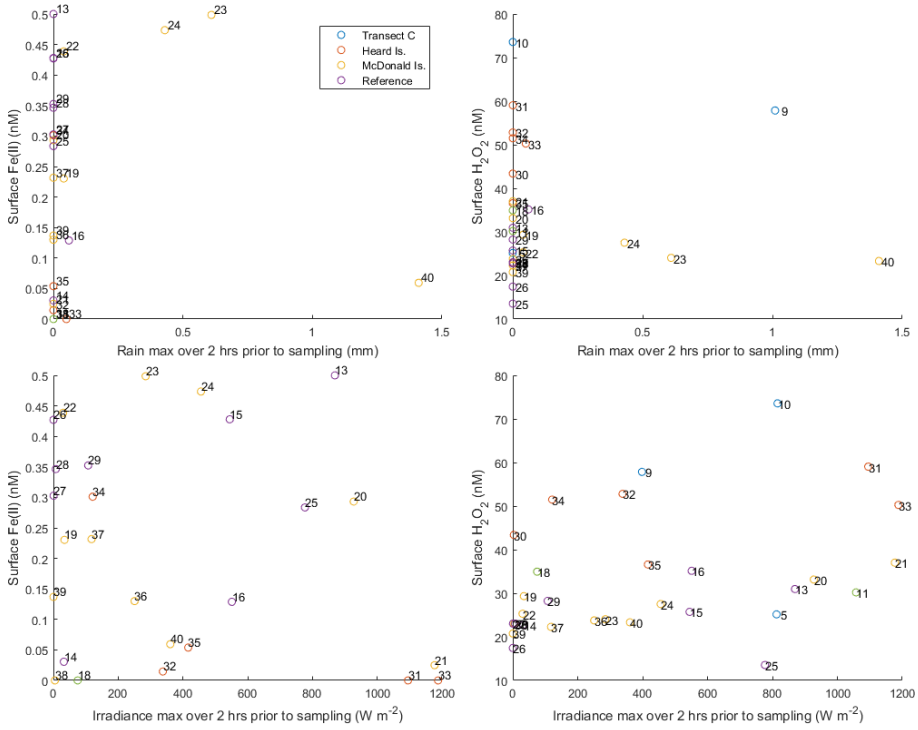

Figure S1. Surface DFe(II) and H_2O_2 vs maximum rainfall and maximum irradiance (PAR) over the 2 hours prior to sampling. Stations are annotated and colour coded by region.

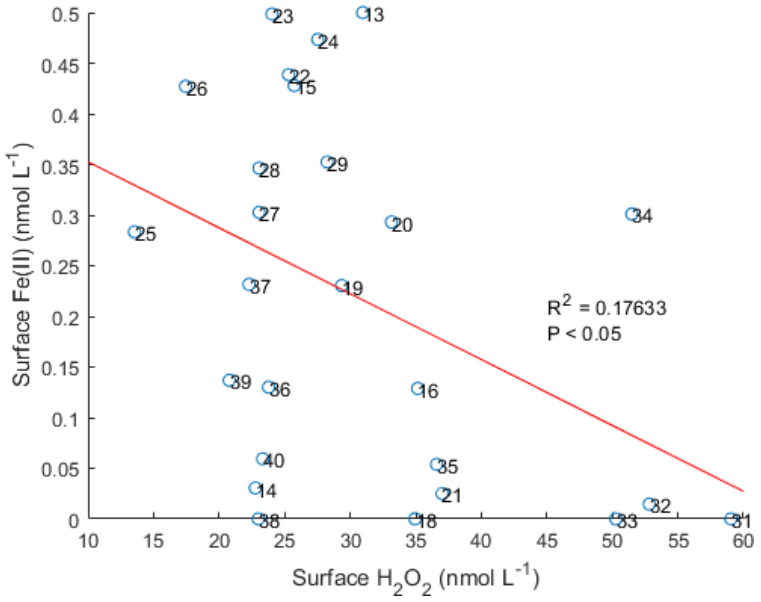

811

812 Figure S2. Surface DFe(II) vs surface H_2O_2 at all stations. Station numbers annotated.